KSME

Springer

Journal of Mechanical Science and Technology 35 (7) 2021

Original Article
DOI 10.1007/s12206-021-0633-x

Keywords:
· Chip formation
· Nickel-phosphorus
· Precision turning
· Relative tool sharpness
· Surface generation

Correspondence to:
Tianfeng Zhou
zhoutf@bit.edu.cn

Citation:
Yu, Q., Zhou, T., He, Y., Liu, P., Wang, X., Yan, J. (2021). Effects of relative tool sharpness on surface generation mechanism of precision turning of electroless nickel-phosphorus coating. Journal of Mechanical Science and Technology 35 (7) (2021) 3113~3121.
http://doi.org/10.1007/s12206-021-0633-x

Received December 16th, 2020
Revised March 4th, 2021
Accepted March 31st, 2021

† Recommended by Editor Hyung Wook Park

Effects of relative tool sharpness on surface generation mechanism of precision turning of electroless nickel-phosphorus coating

Qian Yu[1,2], Tianfeng Zhou[1,3], Yupeng He[1], Peng Liu[1,3], Xibin Wang[1,3] and Jiwang Yan[2]

[1]Key Laboratory of Fundamental Science for Advanced Machining, Beijing Institute of Technology, Beijing 100081, China, [2]Department of Mechanical Engineering, Faculty of Science and Technology, Keio University, Yokohama 2238522, Japan, [3]Beijing Institute of Technology Chongqing Innovation Center, Chongqing 401120, China

Abstract Relative tool sharpness (RTS) is identified as the ratio of undeformed chip thickness to tool cutting edge radius. This paper studies the effects of RTS on the surface generation mechanism of precision turning of electroless nickel-phosphorus (Ni-P) coating. An R-shaped tungsten carbide (WC) tool was adopted for the face turning experiment. The cutting edge radius was 1.84 μm measured by a laser scanning confocal microscope (LSCM). The chip formation behavior, cutting forces and surface morphology were investigated under different RTS values. Results showed that the chip changes from continuous to discontinuous as RTS decreases from 0.54 to 0.27, indicating the transition of the material removal mechanism. The periodical fluctuations with small amplitudes on the machined surface are associated with the high-frequency tool-tip vibration. The low-frequency fluctuations of the cutting forces are related to the material swelling and recovery. The optimal machined surface roughness was obtained at the RTS of 0.38.

1. Introduction

Nickel-phosphorus (Ni-P) coating prepared by the electroless deposition technique was promoted to practical application in 1946 by Brenner and Riddell [1]. The high phosphorus content coating exhibits high hardness, good corrosion resistance, and antiwear property [2-4], which has been used as the mold material for manufacturing optical parts [5-8]. Precision machining is introduced to obtain the Ni-P mold with high surface quality and form accuracy [5]. Since the undeformed chip thickness T in precision machining is in micro- or nano-scale, which is comparable to the tool cutting edge radius r, the effect of cutting edge radius on the machining process cannot be ignored. However, the cutting edge radius effect is ambiguous. To quantify its importance, relative tool sharpness (RTS) has been defined by researchers as the ratio of T to r [9, 10].

A large number of studies based on orthogonal cutting have been conducted to investigate the RTS effect. Sharma et al. [11] found that varying RTS causes different material removal mechanisms, changes in cutting forces and substrate deformation in the nano-scale cutting of Cu by molecular dynamics simulation. Rahman et al. [12] investigated the influence of RTS on ultra-precision machining of magnesium alloy. Results showed that RTS is the most dominant parameter for achieving high surface quality. Kalkhoran et al. [13] demonstrated the importance of RTS in nanometric cutting of mono-crystalline silicon. Under a certain cutting edge radius, the effective rake angle can be changed by applying different undeformed chip thicknesses, resulting in three distinct material removal behaviors in front of the tool edge: shearing, ploughing, and rubbing [10, 14-17]. Variations of material removal mechanism and cutting forces will finally affect the quality of the machined surface. However, the workpiece materials in these

studies are usually magnesium alloys, aluminum alloys, silicon, titanium alloys, and Ni-based superalloys. Few researches have been devoted to studying the effect of RTS on the precision turning of electroless Ni-P.

On the other hand, measuring the tool cutting edge is still challenging because there is no international standard. The geometry of the tool edge is generally considered as an arc between the rake face and the flank face, which is characterized by an edge radius. Both scanning electron microscope (SEM) and atomic force microscope (AFM) have been utilized for the measurement [18, 19]. However, SEM image is a 2-D projection of a 3-D object. If necessary, a reliable cross-section of the tool is required to ensure measurement accuracy. AFM is an effective method with high resolution, but it places strict demands on the operating environment and faces the tip alignment problem. While laser scanning confocal microscope (LSCM) utilizes a confocal scanning imaging technique, which is a high-precision non-contact method that is applicable for measuring the 3-D profile of the cutting edge [16].

Therefore, this paper aims to study the effects of RTS on the surface generation mechanism of precision turning of electroless Ni-P coating. An R-shaped tool was used for the face turning experiment, the cutting edge radius of which was measured by LSCM. Since the R-shaped tool made the chip thickness differs along the cutting edge, a mathematical model was established to describe the variation. The chip formation behavior, cutting forces variation and machined surface morphology were analyzed after the face turning experiment under different RTS values.

2. Experimental procedures

2.1 Cutting edge radius measurement

Similar to Ni-based superalloys, electroless deposited Ni-P is also a difficult-to-machine material. Although single point diamond tool is widely used in precision machining, its nanometric cutting edge radius cannot be accurately detected by LSCM due to the insufficient lateral resolution caused by light diffraction [20]. Considering the problem above, an uncoated R-shaped tungsten carbide (WC) tool (PR13, Kyocera, Japan) with high hardness and excellent toughness was chosen for the precision turning of electroless Ni-P. The tool nose radius is 3.91 mm, the rake angle is 0°, and the clearance angle is 23°.

The tool-tip was scanned by an LSCM (LEXT OLS4000, Olympus, Japan) with a lateral resolution of 120 nm and a vertical resolution of 10 nm. The scanning distance along the cutting edge was 260 μm. As shown in Fig. 1, five section curves with an interval of 40 μm were analyzed. The points on the cutting edge between the rake face and the flank face were marked by stars, and their coordinates were extracted. Then, the cutting edge radius was calculated by MATLAB using the least-squares fitting method. In this paper, the cutting edge radius *r* is assumed to be uniform along the cutting edge. After calculating, an average value of 1.84 μm was obtained, which is acceptable based on a reference value of approximately

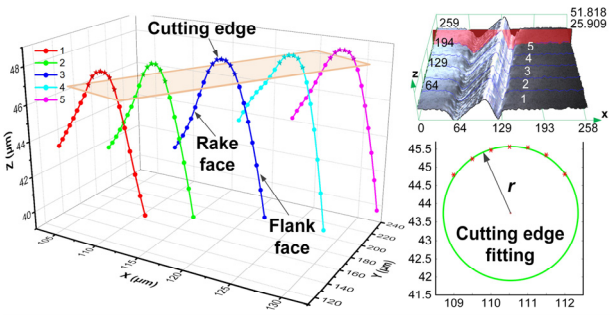

Fig. 1. Measurement of the tool cutting edge radius.

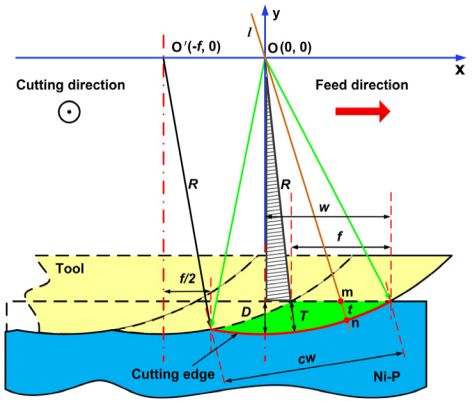

Fig. 2. Schematic diagram of the precision turning model.

2 μm provided by the tool producer.

2.2 Experimental setup

Inspired by Yan et al. [21] and Kalkhoran et al. [13], a precision turning model perpendicular to the cutting direction was developed. The schematic diagram is shown in Fig. 2, where *R* refers to the tool nose radius, *f* refers to the feed rate, *w* refers to the half-width of the engaged tool, and *D* refers to the depth of cut. *w* can be calculated by Eq. (1):

$$w = \sqrt{2RD - D^2}\ . \tag{1}$$

The green part represents the theoretical cross-section of the chip. Chip thickness *t* is the distance between points m and n, which are the intersections of line *l* with the loci of circle O' and circle O, or the loci of workpiece surface and circle O. The slope of line *l* is set to *a*. After the detailed calculation procedure given in the appendix of the present paper, the chip thickness *t* can be determined by Eqs. (2)-(5):

When the range of *a* is $(-\infty, -(R-D)/(w-f)]$,

$$t = R + \frac{f - \sqrt{R^2a^2 - f^2a^2 + R^2}}{\sqrt{a^2+1}}\ . \tag{2}$$

When the range of *a* is $(-(R-D)/(w-f), -(R-D)/w]$,

Table 1. Cutting experiment conditions.

Feed rate *f* (mm/min)	70	62	54	46	39	32
Cutting speed *s* (m/s)	1					
Depth of cut *D* (μm)	2					
Max. undeformed chip thickness *T* (μm)	1.0	0.9	0.8	0.7	0.6	0.5
Theoretical chip width *cw* (μm)	143.4	141.3	139.2	137.1	135.3	133.4
RTS	0.54	0.49	0.43	0.38	0.33	0.27

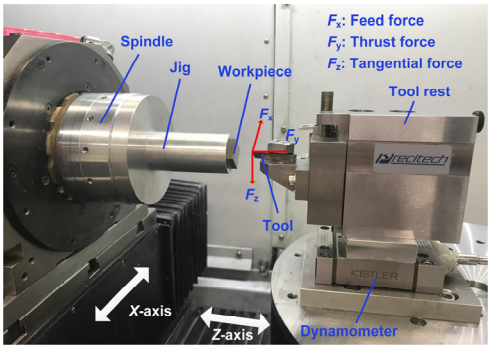

Fig. 3. Experimental setup on the ultra-precision machining center.

$$t = R - \frac{(D-R)\sqrt{a^2+1}}{a}. \tag{3}$$

When the range of a is $[(4R^2-f^2)^{1/2}/f, +\infty)$,

$$t = R - \frac{f + \sqrt{R^2a^2 - f^2a^2 + R^2}}{\sqrt{a^2+1}}. \tag{4}$$

When a is $\pm\infty$,

$$t = R - \sqrt{R^2 - f^2}. \tag{5}$$

T refers to the maximum undeformed chip thickness when a is $-(R-D)/(w-f)$. cw refers to the theoretical chip width. When f is less than w, T can be determined by Eq. (6), and cw can be derived from Eq. (7):

$$T = R - \sqrt{R^2 + f^2 - 2wf}, \tag{6}$$

$$cw = R\sqrt{2\left[1 - \cos\left(\sin^{-1}\frac{f}{2R} + \sin^{-1}\frac{w}{R}\right)\right]}. \tag{7}$$

In the cutting experiment, face turning was conducted on the workpiece surface without cutting fluid by utilizing an ultra-precision machining center (Nanoform X, AMETEK Precitech, USA). Fig. 3 shows the experimental setup. The workpiece was placed on the jig by wax. Before the experiment, the workpiece end surface was flattened to eliminate the tilt caused by the wax. The tool rest was installed on a multicomponent dynamometer (Type 9256C2, Kistler, Switzerland) that applied a sampling frequency of 5 kHz. The cutting force detected at the tool-tip was divided into three components. F_x, F_y, and F_z corresponded to the feed force, thrust force, and tangential force respectively. During the face turning, the feed motion was achieved by the X-axis movement, and the depth of cut was controlled by the Z-axis movement.

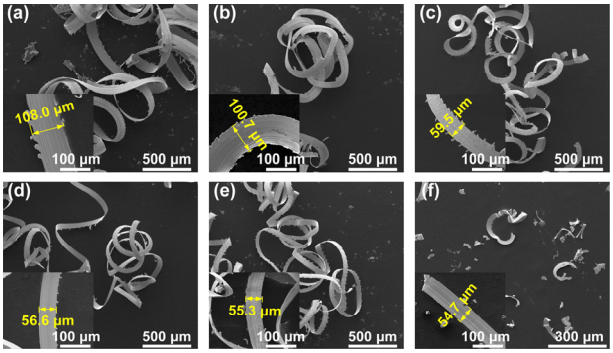

Fig. 4. Chip types at different RTS values: (a) 0.54; (b) 0.49; (c) 0.43; (d) 0.38; (e) 0.33; (f) 0.27.

Table 1 lists the detailed experiment conditions. The cutting speed was set to a moderate value of 1 m/s to avoid the built-up edge generation at low cutting speeds and the workpiece material embrittlement at high cutting speeds [22, 23]. Different max. undeformed chip thicknesses and theoretical chip widths were obtained by feed rate adjustments.

2.3 Characterization

After machining, the cutting chips and the machined surface morphology were observed by utilizing an environmental scanning electron microscope (Inspect S50 ESEM, FEI, USA). The chip width was measured by an imaging processing software (ImageJ, National Institute of Health, USA). The machined surface roughness was measured, and the surface profiles along the cutting and feed directions were detected by LSCM. The fast Fourier transform (FFT) analysis was implemented by a data analysis software (OriginPro 2016, OriginLab, USA).

3. Results and discussion

3.1 Chip formation behavior

Fig. 4 shows the SEM images of the chip types at different RTS values. The chip changes macroscopically from the form of continuous ribbons to segmented pieces as RTS decreases from 0.54 to 0.27. High magnification images shown by the insets reveal serrations along the chip side. They are found on both sides of the chip in Figs. 4(a)-(c) when RTS is larger. As RTS decreases, they are only found on one side, as shown in Figs. 4(d) and (e). In Fig. 4(f), no serrations are found.

Taking the serrations into account, the experimental chip width was measured by the imaging processing software. The comparison of theoretical chip width and experimental chip

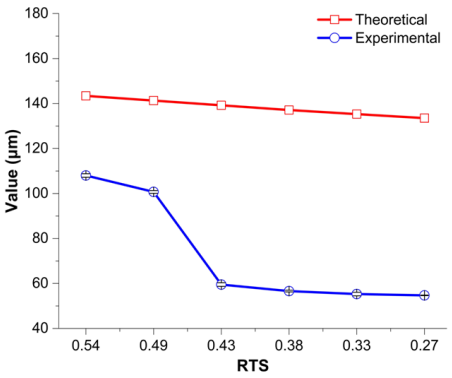

Fig. 5. Comparison of theoretical chip width and experimental chip width.

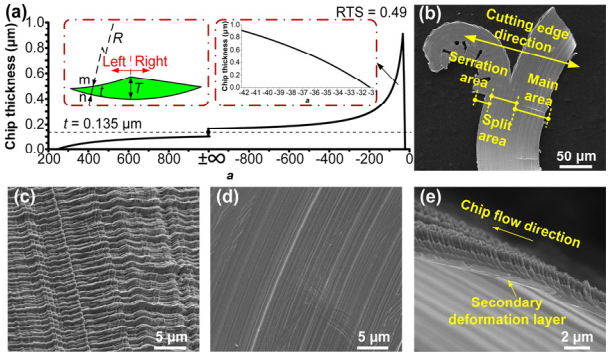

Fig. 6. (a) Chip thickness variation; (b) chip split along the cutting edge; and microstructures of the (c) free surface; (d) back surface; (e) chip side at the RTS of 0.49.

width is shown in Fig. 5. Although both lines display decreasing trend as RTS decreases, the experimental result is much smaller than the theoretical result. Moreover, the experimental value shows a sharp decrease when RTS decreases from 0.49 to 0.43, which reflects an abrupt change of the cutting condition.

The chip thickness variation along the cutting edge at the RTS value of 0.49 is shown in Fig. 6(a). The variation results in different cutting conditions at different positions. At the edge, the thickness is extremely small. The large negative rake angle causes strong friction between the tool and the workpiece material. The material removal mechanism alternates between ploughing and rubbing, and the material side flow leads to the generation of serrations. The thickness is relatively large at the center, where shearing removes the material. As shown in Fig. 6(b), this area is labeled as the main area.

A split area is assumed to exist between the serration area and the main area, where the material removal mechanism difference produces shear stress and tears the chip apart. However, due to the asymmetry of the chip thickness on the left and right sides, the split first occurs on one side; therefore, the edge serrations are only noticed on the other side of the chip. As RTS continues to decrease, the split occurs on both sides, leaving the main area with no serrations. This can explain the chip morphology shown by the insets in Fig. 4. Besides, since the chip splits into many sections along the cutting

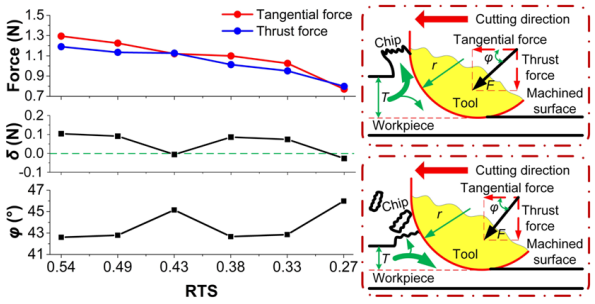

Fig. 7. Experimental cutting force at different RTS values.

edge, the chip width measured in Fig. 5 is only from one section of the chip, thus resulting in a big difference between the theoretical value and the experimental value.

SEM images at high magnifications showing the detailed microstructure of the main area of the chip at the RTS of 0.49 are shown in Figs. 6(c)-(e). SEM images of other RTS values are shown in Fig. A.1 in the Appendix. Lamellar structures [24-28] in the direction perpendicular to the chip flow can be observed at the free surface shown in Fig. 6(c). Since shearing removes the material in the main area, the existence of these uniform lamellar structures results from cyclic shear localization [28]. In contrast, the back surface of the chip shown in Fig. 6(d) is very smooth due to the strong friction with the tool rake face. Some paralleled fringes are noticed along the chip flow direction. The severe shear force caused by the friction between the chip back surface and the tool rake face causes a secondary deformation layer [29] beneath the smooth surface as labeled by the arrow in Fig. 6(e).

3.2 Cutting force variation

The variations of tangential force and thrust force with RTS are shown in Fig. 7. The force decreases as RTS decreases. δ represents the difference between the tangential force and the thrust force, i.e., the value of the tangential force minus that of the thrust force. The value of δ decreases and changes from positive to negative as RTS decreases. F is the resultant force of the tangential force and the thrust force. φ represents the angle between F and the cutting direction, which shows an increasing tendency within the range from 42° to 46° as RTS decreases.

When δ is relatively larger and positive (φ is smaller), most of the deformed material flows upward and forms the chip by shearing. As δ becomes smaller (φ is larger), the significant downward flow of the deformed material occurs, resulting in material swelling and recovery [30]. The negative values of δ and the large values of φ are noticed at the RTS values of 0.43 and 0.27. The material removal mechanism turns into ploughing or rubbing in these cases, giving rise to catastrophic damage to the machined surface.

Fig. 8(a) shows that the cutting forces reveal obvious fluctuations. After FFT analysis, the power spectrum density (PSD) plots are displayed in Figs. 8(b)-(g). Limited to the sampling

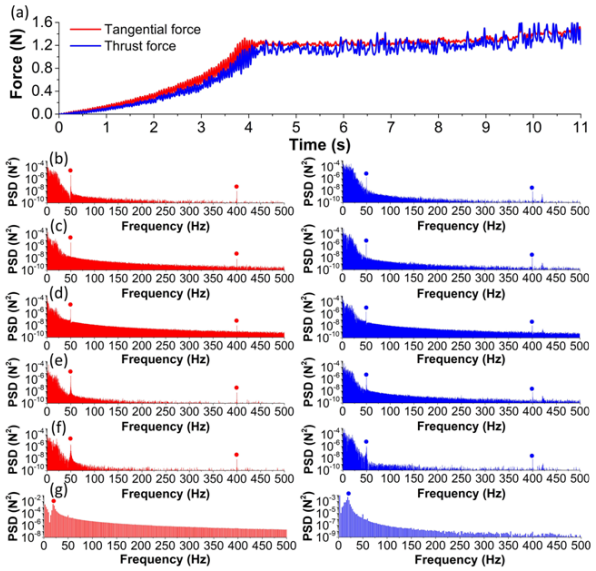

Fig. 8. (a) Experimental cutting force components with time at the RTS of 0.49; and the FFT results of the forces at different RTS values: (b) 0.54; (c) 0.49; (d) 0.43; (e) 0.38; (f) 0.33; (g) 0.27.

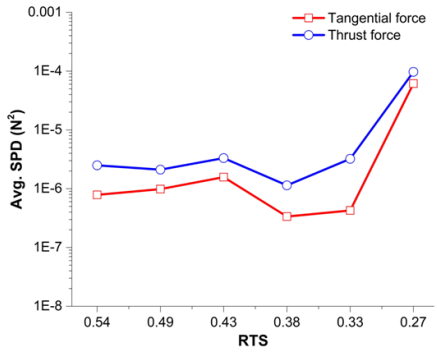

Fig. 9. Average PSD values of cutting forces at different RTS values.

frequency (5 kHz), only the frequencies below 2.5 kHz were accurately calculated in the FFT according to the Nyquist theory. The characteristic peaks of both the tangential force and the thrust force appear at the frequencies of 50 and 400 Hz when RTS ranges from 0.54 to 0.33. When RTS is 0.27, the corresponding PSD value of each frequency increases significantly, and the characteristic frequency becomes smaller than 25 Hz. The low-frequency fluctuations are related to the material swelling and recovery [31].

The variation of average PSD values of tangential force and thrust force with RTS is shown in Fig. 9. The average PSD value of thrust force is larger than that of tangential force, indicating the tool extrusion on the workpiece material. When RTS is 0.43, the average PSD value is a local extremum, which is attributed to the instantaneous change of cutting condition due to the formation of built-up edge. When RTS is 0.27, the average PSD value is the largest. The material removal mechanism changes to ploughing or rubbing, and material swelling and recovery becomes more intense.

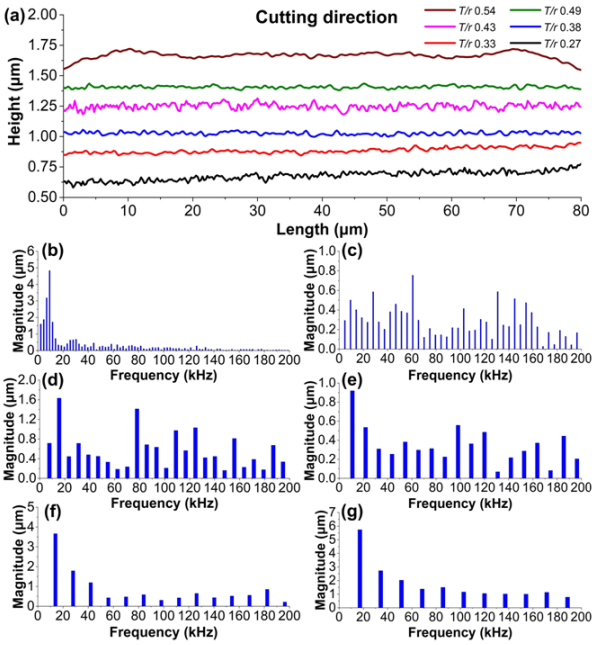

Fig. 10. (a) Surface profiles along the cutting direction; and the corresponding FFT results at different RTS values: (b) 0.54; (c) 0.49; (d) 0.43; (e) 0.38; (f) 0.33; (g) 0.27.

3.3 Machined surface morphology

Fig. 10(a) shows the surface profiles along the cutting direction. Waviness is observed when RTS is 0.54. Profiles of other RTS values seem smooth, but they have small-amplitude high-frequency fluctuations. In comparison, the amplitudes of the fluctuations for the RTS values of 0.43 and 0.27 are slightly larger than those of the others. For the RTS of 0.43, the instantaneous cutting condition variation from the RTS of 0.49 to 0.43 mentioned in the former section might be associated with the result. For the RTS of 0.27, the result arises from the plastic projections on the machined surface caused by the strong friction between the tool cutting edge and the matrix material.

The FFT method was utilized to analyze the surface profile frequency characteristics along the cutting direction. As shown in Figs. 10(b)-(g), characteristic peaks appear at a frequency range from 10 to 20 kHz, which indicates that the machined surface fluctuations are associated with the high-frequency tool-tip vibration [32, 33].

Fig. 11(a) shows the surface profiles along the feed direction. For the profiles at the RTS values of 0.54, 0.49, 0.43, and 0.38, periodical waviness approximately corresponding to the tool feed rate can be easily observed. While the periods are not clear for the profiles at the RTS values of 0.33 and 0.27, big bulges are found due to the chip adhesion on the machined surface as shown in Figs. 11(b) and (c). As RTS decreases, the high temperature caused by strong friction makes both the chip surface and the machined surface active and easy to adhere to each other. As shown in Fig. 11(d), adhesions are found on both the tool rake face and the chip. Moreover, strong

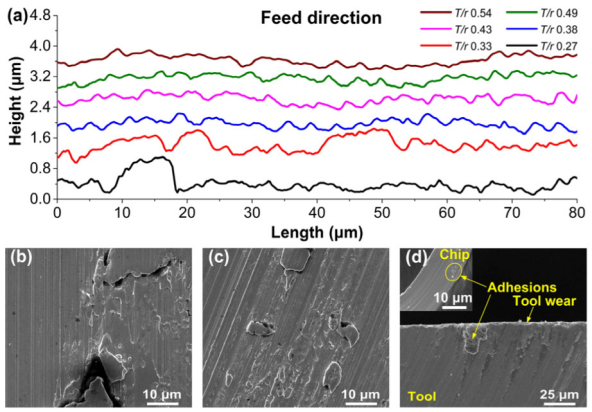

Fig. 11. (a) Surface profiles along the feed direction; and SEM images of (b) the machined surface at the RTS of 0.33; (c) the machined surface at the RTS of 0.27; (d) the adhesions on both the tool and the chip.

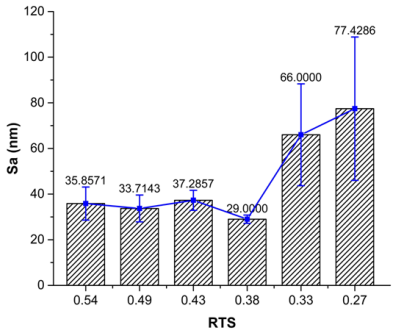

Fig. 12. Surface roughness at different RTS values.

friction also leads to tool wear.

Fig. 12 shows the roughness results of the machined surfaces at different RTS values. The optimal surface roughness with a value of 29 nm can be obtained at the RTS of 0.38. When RTS is larger than 0.38, Sa has a local extremum at the RTS of 0.43 due to the instantaneous change of cutting condition mentioned before. Since the feed rate is decreasing, Sa shows a decreasing trend as RTS decreases. When RTS is smaller than 0.38, Sa increases sharply due to the adhesions on the machined surface.

4. Conclusion

The present paper studied the RTS effects on the surface generation mechanism of precision turning of electroless Ni-P coating. The face turning experiments under different RTS values were conducted based on an R-shaped WC tool. The tool cutting edge radius was 1.84 μm measured by LSCM. As RTS decreases, the chip gradually changes from the form of continuous ribbons to segmented pieces. Different cutting conditions along the cutting edge due to the chip thickness difference cause the chip serration and the chip split. The effective rake angle is influenced by RTS that determines the shearing and ploughing contributions during the machining process, thereby influencing the surface generation. The low-frequency fluctuations of the cutting forces are related to the material swelling and recovery. While the high-frequency periodical fluctuations with small amplitudes on the machined surface are governed by the high-frequency tool-tip vibration. The optimal machined surface quality with a Sa of 29 nm is obtained at the RTS of 0.38.

Acknowledgments

This work was supported by the National Basic Research Program of China (grant number 2015CB059900), the National Natural Science Foundation of China (grant numbers 51775046, 51875043, and 52005040), Beijing Municipal Natural Science Foundation (grant number JQ20014) and China Postdoctoral Science Foundation (grant number 2019 M660480). Qian Yu acknowledges the financial support from China Scholarship Council (CSC) for his visiting research in Japan.

Nomenclature

a	: Slope of the line
cw	: Theoretical chip width
D	: Depth of cut
f	: Feed rate
F	: Resultant force of F_z and F_y
F_x	: Feed force
F_y	: Thrust force
F_z	: Tangential force
r	: Cutting edge radius
R	: Tool nose radius
s	: Cutting speed
Sa	: Surface roughness
t	: Chip thickness
T	: Undeformed chip thickness
w	: Half-width of the engaged tool
x_m	: Abscissa of point m
x_n	: Abscissa of point n
y_m	: Ordinate of point m
y_n	: Ordinate of point n
δ	: Difference between F_z and F_y
φ	: Angle between F and the cutting direction

References

[1] A. Brenner and G. E. Riddell, Nickel plating on steel by chemical reduction, *Journal of Research of the National Bureau of Standards*, 37 (1) (1946) 31-34.

[2] Q. Yu et al., Annealed high-phosphorus electroless Ni-P coatings for producing molds for precision glass molding, *Materials Chemistry and Physics*, 262 (2021) 124297.

[3] C. Cui et al., Corrosion behavior of the electroless Ni-P coating on the pore walls of the lotus-type porous copper, *Corrosion Science*, 162 (2020) 108202.

[4] I. Saravanan et al., Wear behaviour of electroless Ni-P and Ni-P-TiO_2 composite coatings on En8 steel, *Materials Today: Proceedings*, 22 (2020) 1135-1139.
[5] T. Zhou et al., Recent advancements in optical microstructure fabrication through glass molding process, *Frontiers of Mechanical Engineering*, 12 (1) (2017) 46-65.
[6] X. Lan et al., Deformation analysis and improvement method of the Ni-P mold core in the injection molding process, *International Journal of Advanced Manufacturing Technology*, 99 (9-12) (2018) 2659-2668.
[7] J. Xie et al., Research on rhenium-iridium alloy coating on microgroove molds in precision glass molding, *Applied Nanoscience* (2019).
[8] N. Milan et al., Effects of micromilled NiP mold surface topography on the optical characteristics of injection molded prismatic retroreflectors, *Precision Engineering*, 61 (2020) 126-135.
[9] J. C. Outeiro and V. P. Astakhov, The role of the relative tool sharpness in modelling of the cutting process, *Proceedings of the 8th CIRP International Workshop on Modelling of Machining Operations,* Chemnitz, Germany (2005) 517-524.
[10] M. A. Rahman et al., Variation of surface generation mechanisms in ultra-precision machining due to relative tool sharpness (RTS) and material properties, *International Journal of Machine Tools and Manufacture*, 115 (2017) 15-28.
[11] A. Sharma et al., Investigation of effect of uncut chip thickness to edge radius ratio on nanoscale cutting behavior of single crystal copper: MD simulation approach, *Journal of Micromanufacturing* (2020) 1-12.
[12] M. A. Rahman et al., Influence of relative tool sharpness (RTS) on different ultra-precision machining regimes of Mg alloy, *International Journal of Advanced Manufacturing Technology*, 96 (2018) 3545-3563.
[13] S. N. A. Kalkhoran et al., Effect of relative tool sharpness on subsurface damage and material recovery in nanometric cutting of mono-crystalline silicon: a molecular dynamics approach, *Materials Science in Semiconductor Processing*, 108 (2020) 104868.
[14] F. Xu et al., A study on the tool edge geometry effect on nano-cutting, *International Journal of Advanced Manufacturing Technology*, 91 (2017) 2787-2797.
[15] F. Fang and F. Xu, Recent advances in micro/nano-cutting: effect of tool edge and material properties, *Nanomanufacturing and Metrology*, 1 (2018) 4-31.
[16] Q. Shen et al., Effects of cutting edge microgeometry on residual stress in orthogonal cutting of inconel 718 by FEM, *Materials*, 11 (6) (2018) 1015.
[17] N. Jeyaprakash et al., Minimum cutting thickness and surface roughness achieving during micromachining of aluminium 19000 using CNC machine, *Materials Today: Proceedings*, 21 (2020) 755-761.
[18] M. Akbari et al., Comparison of transparent objects metrology through diamond cutting edge radii measurements, *CIRP Journal of Manufacturing Science and Technology*, 13 (2016) 72-84.
[19] Y. L. Chen et al., An edge reversal method for precision measurement of cutting edge radius of single point diamond tools, *Precision Engineering*, 50 (2017) 380-387.
[20] W. Gao et al., Nanometer edge profile measurement of diamond cutting tools by atomic force microscope with optical alignment sensor, *Precision Engineering*, 30 (4) (2006) 396-405.
[21] J. Yan et al., Mechanism for material removal in diamond turning of reaction-bonded silicon carbide, *International Journal of Machine Tools and Manufacture*, 49 (5) (2009) 366-374.
[22] B. Wang et al., Influences of cutting speed and material mechanical properties on chip deformation and fracture during high-speed cutting of inconel 718, *Materials*, 11 (4) (2018) 461.
[23] R. Kumar et al., Hard turning on JIS S45C structural steel: an experimental, modelling and optimisation approach, *International Journal of Automotive and Mechanical Engineering*, 16 (4) (2019) 7315-7340.
[24] M. Q. Jiang and L. H. Dai, Formation mechanism of lamellar chips during machining of bulk metallic glass, *Acta Materialia*, 57 (9) (2009) 2730-2738.
[25] M. A. Rahman et al., Investigation of the critical cutting edge radius based on material hardness, *International Journal of Advanced Manufacturing Technology*, 88 (9-12) (2017) 3295-3306.
[26] B. Davis et al., Chip morphology and chip formation mechanisms during machining of ECAE-processed titanium, *Journal of Manufacturing Science and Engineering*, 140 (3) (2017) 031008.
[27] X. Fu et al., The influence of hydrogen on chip formation in cutting Ti-6Al-4V alloys, *International Journal of Advanced Manufacturing Technology*, 89 (1-4) (2017) 371-375.
[28] S. Zhang et al., Cyclic shear angle for lamellar chip formation in ultra-precision machining, *Proceedings of the Institution of Mechanical Engineers, Part C: Journal of Mechanical Engineering Science*, 234 (13) (2020) 2673-2680.
[29] J. Yan et al., Chip formation behaviour in ultra-precision cutting of electroless nickel plated mold substrates, *Key Engineering Materials*, 257-258 (2004) 3-8.
[30] W. S. Yip and S. To, Reduction of material swelling and recovery of titanium alloys in diamond cutting by magnetic field assistance, *Journal of Alloys and Compounds*, 722 (2017) 525-531.
[31] S. J. Zhang et al., A review of surface roughness generation in ultra-precision machining, *International Journal of Machine Tools and Manufacture*, 91 (2015) 76-95.
[32] H. Wang et al., Investigation on the influence of tool-tip vibration on surface roughness and its representative measurement in ultra-precision diamond turning, *International Journal of Machine Tools and Manufacture*, 69 (2013) 20-29.
[33] W. S. Yip and S. To, Reduction of tool tip vibration in single-point diamond turning using an eddy current damping effect, *International Journal of Advanced Manufacturing Technology*, 103 (5-8) (2019) 1799-1809.

Appendix

A. Calculation of the chip thickness

As shown in Fig. 2, a Cartesian coordinate system is established with O as its origin. Thus, the locus equation of circle O is

$$x^2 + y^2 = R^2 , \tag{A.1}$$

and the locus equation of circle O' is

$$(x + f)^2 + y^2 = R^2 . \tag{A.2}$$

The green part represents the theoretical chip shape. Chip thickness *t* is defined as the distance between points m and n. The slope of line *l* is set to *a*, the ranges of which are [-∞, -(*R*-*D*)/*w*] and [$(4R^2-f^2)^{1/2}$/*f*, +∞].

When the ranges of *a* are [-∞, -(*R*-*D*)/(*w*-*f*)] and [$(4R^2-f^2)^{1/2}$/*f*, +∞], the coordinates of points m and n can be calculated by Eq. (A.3):

$$\begin{cases} \begin{bmatrix} (x+f)^2 + y^2 = R^2 \\ ax - y = 0 \end{bmatrix} \\ \begin{bmatrix} x^2 + y^2 = R^2 \\ ax - y = 0 \end{bmatrix} \end{cases} . \tag{A.3}$$

When the range of *a* is (-(*R*-*D*)/(*w*-*f*), -(*R*-*D*)/*w*], the coordinates can be calculated by Eq. (A.4):

$$\begin{cases} \begin{bmatrix} y + R - D = 0 \\ ax - y = 0 \end{bmatrix} \\ \begin{bmatrix} x^2 + y^2 = R^2 \\ ax - y = 0 \end{bmatrix} \end{cases} . \tag{A.4}$$

After calculation, the coordinates of points m and n are as follows:

$$\begin{cases} \begin{bmatrix} x_m = -\dfrac{f + \sqrt{R^2(a^2+1) - a^2 f^2}}{a^2+1} \\ y_m = \dfrac{a(-f + \sqrt{R^2(a^2+1) - a^2 f^2})}{a^2+1} \end{bmatrix} , a \in \left[-\infty, -\dfrac{R-D}{w-f} \right] , \\ \begin{bmatrix} x_n = \dfrac{R}{\sqrt{a^2+1}} \\ y_n = \dfrac{aR}{\sqrt{a^2+1}} \end{bmatrix} \end{cases} \tag{A.5}$$

$$\begin{cases} \begin{bmatrix} x_m = \dfrac{D-R}{a} \\ y_m = D - R \end{bmatrix} \\ \begin{bmatrix} x_n = \dfrac{R}{\sqrt{a^2+1}} \\ y_n = \dfrac{aR}{\sqrt{a^2+1}} \end{bmatrix} , a \in \left(-\dfrac{R-D}{w-f}, -\dfrac{R-D}{w} \right] , \end{cases} \tag{A.6}$$

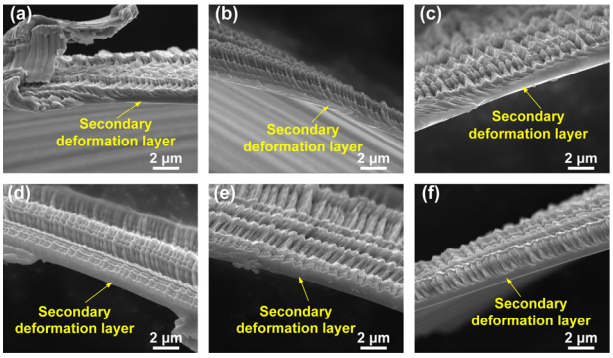

Fig. A.1. Chip structures at different RTS values: (a) 0.54; (b) 0.49; (c) 0.43; (d) 0.38; (e) 0.33; (f) 0.27.

$$\begin{cases} \begin{bmatrix} x_m = -\dfrac{f + \sqrt{R^2(a^2+1) - a^2 f^2}}{a^2+1} \\ y_m = -\dfrac{a(f + \sqrt{R^2(a^2+1) - a^2 f^2})}{a^2+1} \end{bmatrix} , a \in \left[\dfrac{\left(4R^2 - f^2\right)^{\frac{1}{2}}}{f}, +\infty \right] . \\ \begin{bmatrix} x_n = -\dfrac{R}{\sqrt{a^2+1}} \\ y_n = -\dfrac{aR}{\sqrt{a^2+1}} \end{bmatrix} \end{cases} \tag{A.7}$$

Therefore, the chip thickness can be determined by Eq. (A.8), and the final results are given by Eqs. (2)-(5).

$$t = \sqrt{(x_m - x_n)^2 + (y_m - y_n)^2} . \tag{A.8}$$

SEM images at high magnifications showing the detailed microstructure of the chips at different RTS values are shown in Fig. A.1.

Qian Yu is currently a Ph.D. candidate at Key Laboratory of Fundamental Science for Advanced Machining, Beijing Institute of Technology, Beijing, China. He received his Bachelor's degree in School of Mechanical Engineering in Beijing Institute of Technology, Beijing, China, in 2015. He studied in Department of Mechanical Engineering in Keio University, Yokohama, Japan, from 2018 to 2019. His research interests include ultra-precision machining, micro- and nano-manufacturing.

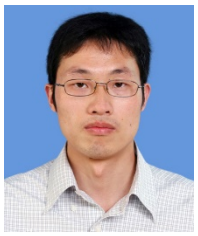

Tianfeng Zhou is currently a Professor and a Ph.D. candidate supervisor at Key Laboratory of Fundamental Science for Advanced Machining, Beijing Institute of Technology, Beijing, China. He received his Ph.D. degree in Tohoku University, Japan, in 2009. He worked as an Assistant Professor in Tohoku University, Japan, from 2010 to 2012. His main research interests include extreme manufacturing, precision glass molding, mold material development, optical engineering, micro- and nano-manufacturing.